SANDIA REPORT

SAND2016-9537
Unlimited Release
September 2016

Exploration of Two-Dimensional Materials for Remote Sensing Applications

James A. Bartz
Isaac Ruiz
Steve Howell
Shiyuan Gao
Michael Thomas
Jessica Depoy

Prepared by
Sandia National Laboratories
Albuquerque, New Mexico 87185 and Livermore, California 94550

Sandia National Laboratories is a multi-mission laboratory managed and operated by Sandia Corporation, a wholly owned subsidiary of Lockheed Martin Corporation, for the U.S. Department of Energy's National Nuclear Security Administration under contract DE-AC04-94AL85000.

Issued by Sandia National Laboratories, operated for the United States Department of Energy by Sandia Corporation.

Available to DOE and DOE contractors from
U.S. Department of Energy
Office of Scientific and Technical Information
P.O. Box 62
Oak Ridge, TN 37831

Telephone: (865) 576-8401
Facsimile: (865) 576-5728
E-Mail: reports@osti.gov
Online ordering: http://www.osti.gov/scitech

Available to the public from
U.S. Department of Commerce
National Technical Information Service
5301 Shawnee Rd
Alexandria, VA 22312

Telephone: (800) 553-6847
Facsimile: (703) 605-6900
E-Mail: orders@ntis.gov
Online order: http://www.ntis.gov/search

SAND2016-9537
Unlimited Release
September 2016

Exploration of Two-Dimensional Materials for Remote Sensing Applications

James A. Bartz, Advanced Sensing Technologies
Isaac Ruiz, Applied Photonic Microsystems
Steve Howell, Applied Photonic Microsystems
Shiyuan Gao, Materials Physics
Michael Thomas, Applied Photonic Microsystems
Jessica Depoy, Advanced Sensing Technologies

Sandia National Laboratories
P.O. Box 5800
Albuquerque, New Mexico 87185-MS0968

Abstract

Two-dimensional materials were explored through collaboration with Steve Howell and Catalyn Spataru, led by James Bartz during FY15 and FY16 at Sandia National Laboratories. Because of their two-dimensional nature, these materials may offer properties exceeding those of bulk materials. This work involved Density Functional Theory simulations and optical methods, instrumentation development, materials growth and materials characterization. Through simulation the wide variety of two dimensional materials was down-selected for fabrication and testing. Out of the two dimensional semiconductors studied, black phosphorus bilayers showed the strongest spectral absorption tuning with applied electric field. Laser scanning confocal microscopy, spectroscopy and atomic force microscopy allowed for identification of micron scale samples. A technique involving conductive tip atomic force microscopy and back-side illumination was developed simple assembly and characterization of material spectral response.

CONTENTS

FIGURES

TABLES

NOMENCLATURE

AFM	Atomic Force Microscopy
BSE	Bethe-Salpeter Equation
CBM	Conduction Band Minimum
DFT	Density Functional Theory
DOE	Department of Energy
DPSS	Diode Pumped Solid State
eV	Electron Volt
GW	Green's function method
HfO_2	Hafnium Oxide
IR	Infrared
ITO	Indium-Tin-Oxide
LDA	Low Density Approximation
LSCM	Laser Scanning Confocal Microscope
MoS_2	Molybdenum disulfide
$MoSe_2$	Molybdenum diselenide
MLG	Multi-Layer Graphene
PBE	Perdew-Burke-Ernzerhof function
SiO_2	Silicon Dioxide
SNL	Sandia National Laboratories
TMDC	Transition Metal Dichalcogenide
TS_2	Titanium disulfide
TSe_2	Titanium diselenide
VBM	Valence Band Maximum
WS_2	Tungsten disulfide
WSe_2	Tungsten diselenide

1. INTRODUCTION

1.1. Detector Physics Motivation

To address the question of what makes a good detector, Kinch developed a figure of merit involving the thermal generation rate G [$m^{-6}s^{-1}$] and the absorption coefficient α [m^{-1}] (Kinch, 2000).For background limited photo detection (BLIP),

$$\eta_a \Phi_B > n_{th} t/\tau$$

where the left side of the inequality represents the photo carrier generation rate per unit area (absorption efficiency times the background signal flux) and the right side represents the thermal generation rate per unit area (thermal carrier density times thickness divided by carrier lifetime). Assuming the quantum efficiency can be expressed as the absorption coefficient multiplied by the detector thickness, the normalized thermal generation rate can be written as

$$G_{th} = n_{th}/\alpha\tau$$

This parameter was suggested because it provides a method for unambiguously predicting the ultimate performance of any IR material. There is a built-in exclusion, however that 1/f noise and excess current sources such as tunnel and thermal generation within the depletion region are unavoidable because they are typically associated with defects in the bandgap. This parameter suggests low rates of thermal carrier generation and large absorption coefficient and large carrier lifetime correlate to good detector materials.

One method to reduce thermal generation is to reduce the volume of the detector material. 2D materials represent the extreme limit of detector thickness. Very high absorption coefficients are required to effectively absorb photons in such thin layers. Monolayer MoS_2 absorbs up 10%, which is significant considering the atomic-scale thickness (Bablu Mukherjee, 2015).

1.2. Materials Modeling

1.2.1. Density Functional Theory Overview

If known, the quantum mechanical wavefunction provides all the information about an atom, molecule or material. The wavefunction for a system as simple as the helium atom can't be solved exactly, so approximations are necessary. Density Functional Theory is a powerful tool for applying such approximations (Sholl & Steckel, 2009).

Schrodinger equation for a collection of atoms and electrons:

$$\left[-\frac{\hbar}{2m}\sum_{i=1}^{N}\nabla_i^2 + \sum_{i=1}^{N}V(\boldsymbol{r}_i) + \sum_{i=1}^{N}\sum_{j<i}U(\boldsymbol{r}_i, r_j)\right]\psi = E\psi$$

In the above equation, m represents the electron mass. The terms in the brackets, from left to right are the kinetic energy, the potential energy and the electron interaction potential. The system is a many body problem. The electron density is calculated by:

$$n(\boldsymbol{r}) = 2\sum_i \psi_i^*(\boldsymbol{r})\psi_i(\boldsymbol{r})$$

Through variational numerical methods, the density can be solved for such that it provides the lowest energy state of the system. This is the basis for density functional theory.

An approximate, non-interacting, absorption spectrum can be obtained by diagonalization of the Hamiltonian and determining the amount of coupling between valence band and conduction band states (Deslippe, Samsonidze, Strubbe, Jain, Cohen, & Louie, 2012). This simple yet powerful method was applied to disregard certain materials while emphasizing further research of others.

1.2.2. Methods

Throughout this work Quantum Espresso was used to solve for the Hamiltonian and wave functions of various two-dimensional materials.

1.3. Modeling Heterostructures

Terrones, López-Urías et al. (2013) performed first principles calculations on different heterostructures of Transition Metal Dichalcogenides (TMDCs), including MoS_2, Ws_2, $MoSe_2$, WSe_2, TS_2 and TSe_2. The heterostructure formed by MoS_2-WSe_2 exhibits the smallest bandgap (Figure 1) out of the structures studied in this paper (Humberto, Lopez-Urias, & Terrones, 2013).

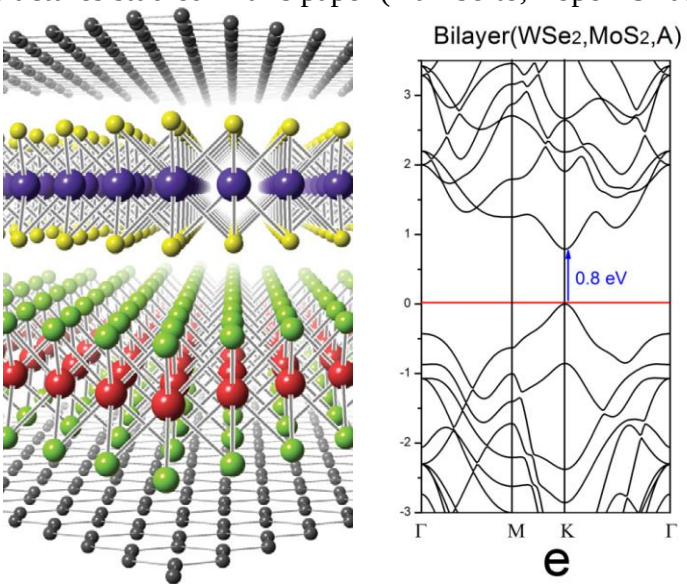

Figure 1 Cartoon of two Monolayer TMDCs surrounded by graphene (Lee, et al., 2014) and the bandstructure of WSe_2-$MoSe_2$ heterostructure (Humberto, Lopez-Urias, & Terrones, 2013).

In order to promote an electron into the conduction band with a photon, the photon must have energy greater than or equal to the bandgap energy. The wavelength associated with this energy is given by:

$$\lambda = \frac{1240}{E_g} \; [nm * eV]$$

To first order approximation, a bandgap of 0.8 eV corresponds to absorption of a of 1550 nm wavelength photon.

This MoS_2-WSe_2 heterostructure has been fabricated and characterized (Lee, et al., 2014). These devices show reasonably high quantum efficiency.

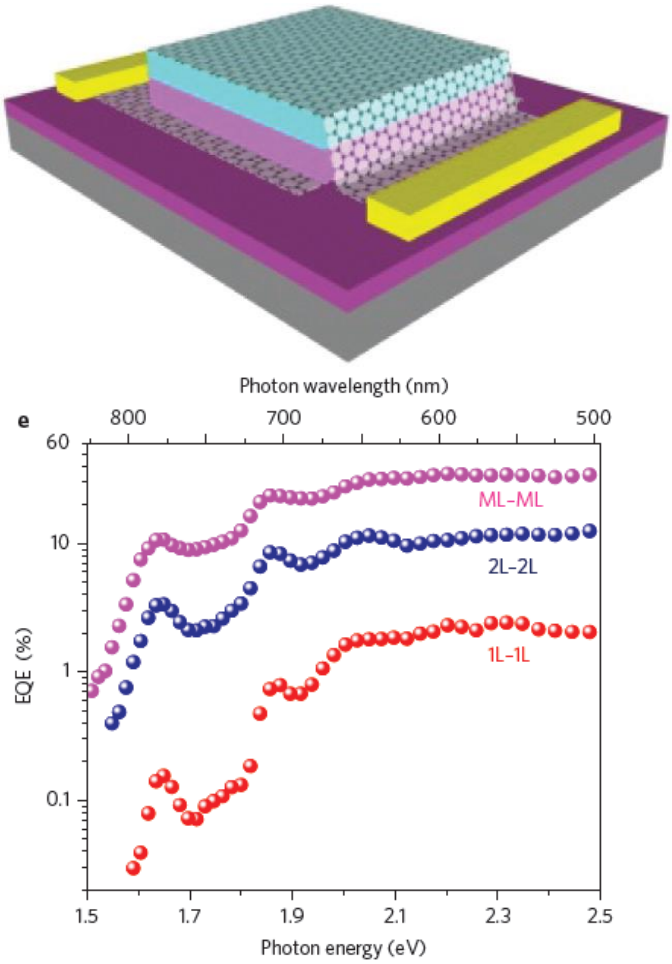

Figure 2 Graphic of device fabricated (top) and correspding absorption spectrum (bottom). Images taken from (Lee, et al., 2014).

Contrary to modeling efforts studying these heterostructures, the bandgap does not decrease when this heterojunction is formed. In Figure 3 the brown curve represents the heterostructure and the red and blue represent the WSe_2 and MoS_2, respectively.

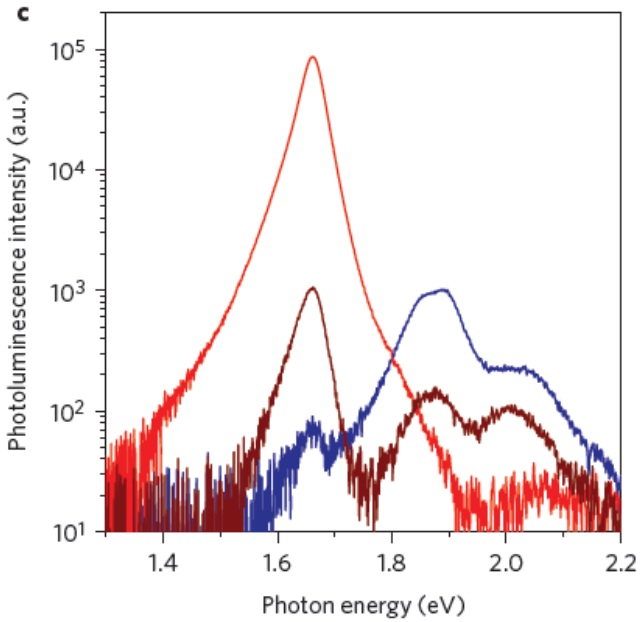

Figure 3 Photoluminescence spectra of MoS_2 monolayer (blue trace), WSe_2 monolayer (red trace) and MoS_2-WSe_2 heterostructure (brown trace) (Lee, et al., 2014).

Reduction in the electronic bandgap was modeled, but experiment did not reproduce the expected result. The following section attempts to describe the discrepancy between the modeling and experiment.

The inputs to DFT simulations include arrangement of atoms, atom types, various cutoff energies and pseudo-potentials. Crystal structures are handled easily because they can be represented in the Fourier domain. An infinite array of atoms is described by a monotonic spatial frequency in each dimension. However, when simulating multiple crystals with differing lattice constants, potentially large numbers (cells) of atoms have to be simulated at high computational cost. A simple approximation is to adjust the lattice constants to make the dissimilar materials easy to simulate together. This approximation returns non-physical results. When strain is introduced into material systems, the properties are altered (Lu, et al., 2014). These strained properties were demonstrated in the modeling. However, when the device was created, the straining did not occur. The materials bonded together by van der Waals forces. During the bonding process the unit cells of the crystals did not shrink and expand to cause unit cells to line up.

The approximation of identical unit cell size fails to represent exfoliation-based heterostructure device properties. The approximation has been applied in several papers. Combining this approach with varied electric field various electric fields to shows electrically tunable properties. However, the effect may be due to the strained nature of the system, as imposed by the modeling, which is difficult to realize in fabrication.

2. MODELING – THIS WORK

2.1. Strained MoS_2- WTe_2

To illustrate the effect of strain on 2D heterostructure calculations, the MoS_2-WTe_2 was selected. Simulated and relaxed with a LDA pseudopotential, MoS_2 has a lattice constant of 3.14 Å, while WTe_2 has a lattice contestant of 3.49 Å. To model these two materials together both lattice constants were expanded/contracted to 3.31 Å. The calculated bandstructures are shown in Figure 4.

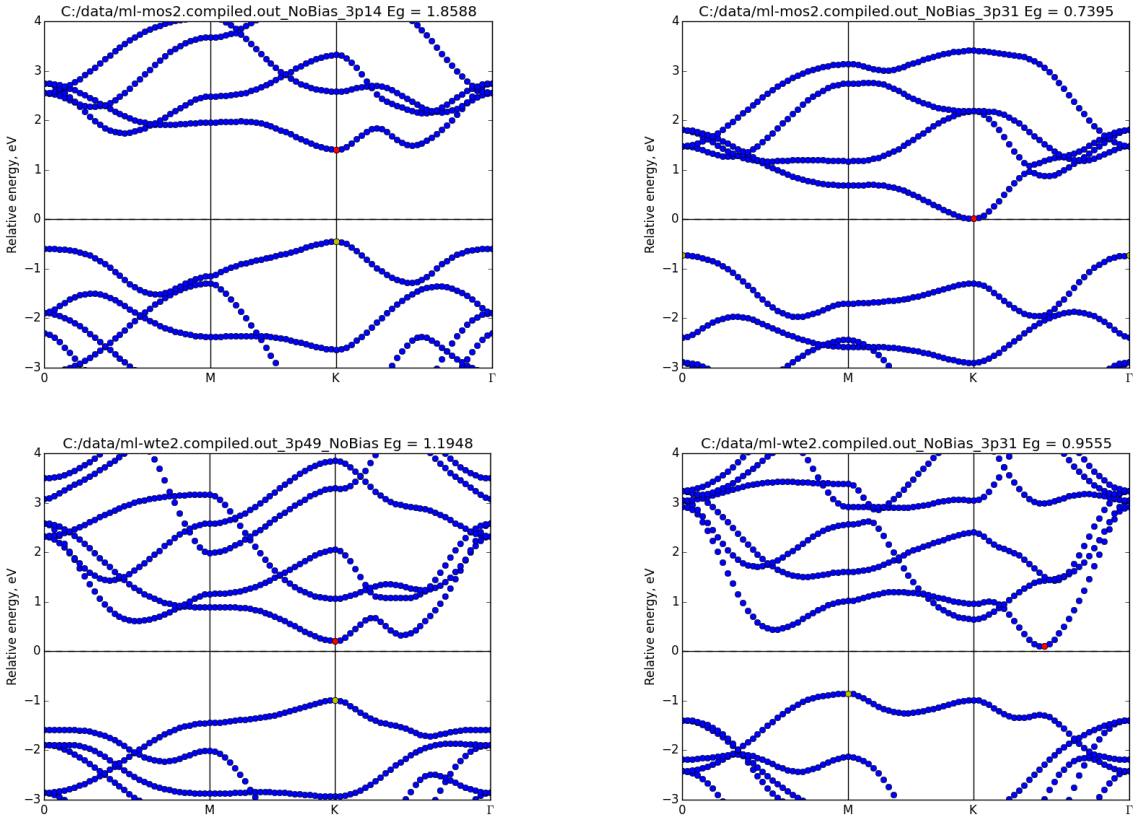

Figure 4 Bandstructures of relaxed and stretched MoS_2 (top-left and top-right) and relaxed and contracted WTe_2 (bottom-left and bottom-right. Both relaxed structures a direct bandgap at the K-point while indirect gaps arise when the lattice constants are modified.

Figure 5 shows that, by this technique, the heterostructure bandgap collapses at the K-point.

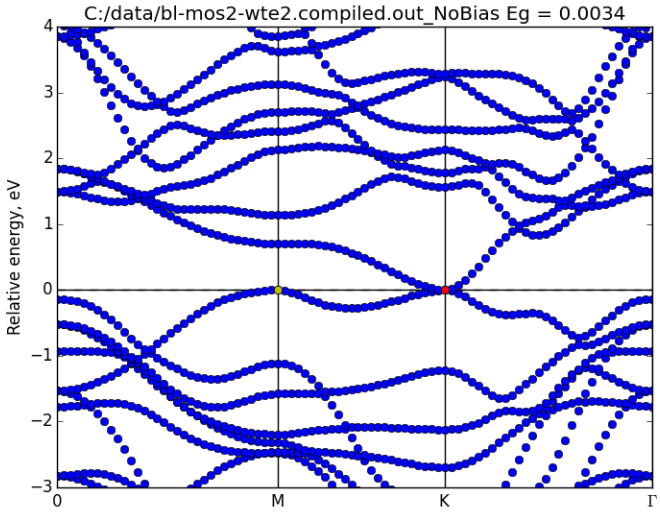

Figure 5 Bandstructure of the MoS_2-WTe_2 heterostructure with a lattice constant of 3.31 angstroms. The bandgap is collapsed.

The results of the DFT calculations were processed to extract an absorption spectrum in the non-many-body / non-interacting approximation and are shown Figure 6 and Figure 7. One might expect a strong transition between low energies because of the collapsed band gap shown in Figure 5. This difference is potentially explained by lack of coupling between electron states between the two layers.

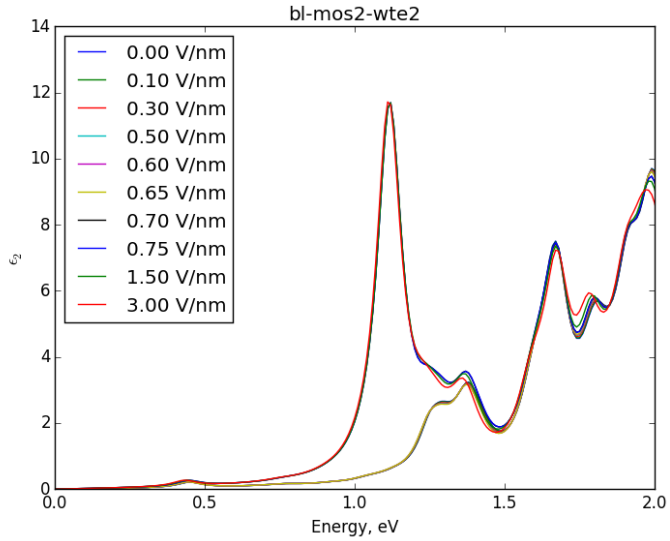

Figure 6 Calculated complex dielectric function as a function of energy. The various trend lines indicate different electric fields applied through these simulations.

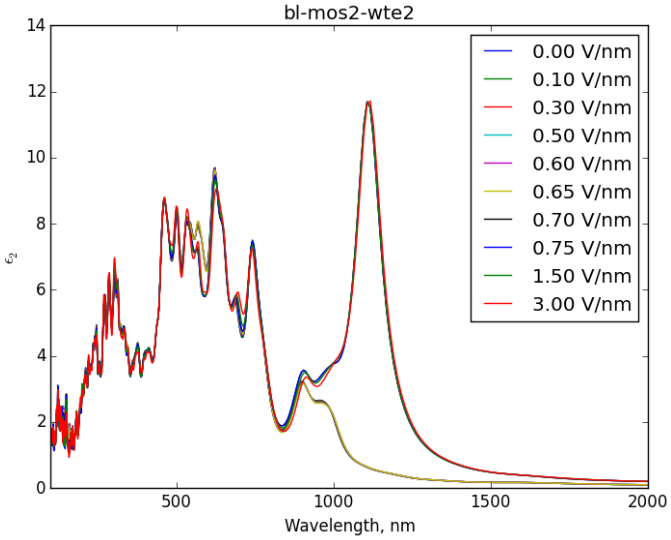

Figure 7 Calculated complex dielectric function as a function of wavelength. The various trend lines indicate different electric fields applied through these simulations.

Another interesting observation in Figure 7 is the strong modification of the absorption spectrum near 1200 nm with electric fields of 0.75 V/nm and higher. A feature like this may attract interest in applications requiring adaptive sensing. However, the simulation involved an approximation (strained lattice) that may result in interesting, although non-physical results. Refined calculations may improve the quality of results but experiment is necessary to confirm.

2.2. Black Phosphorous

While TMDC monolayers, bilayers and heterostructures seem to show variation in the Band Gap with changing electric field, upon calculating the absorption spectrum, the anticipated features were lacking. This may be because of the weakness of interlayer optical transitions. Black phosphorus, however showed band gap modification in the band structure (Figure 8) as well as optical absorption calculations.

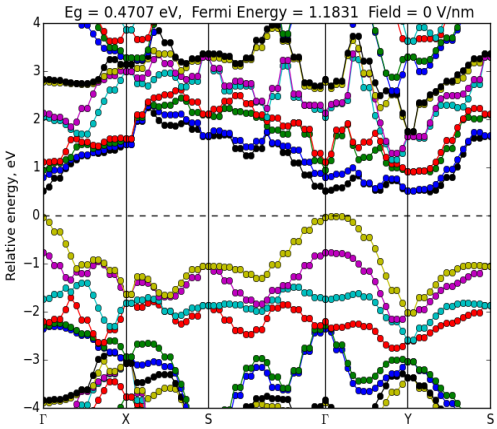

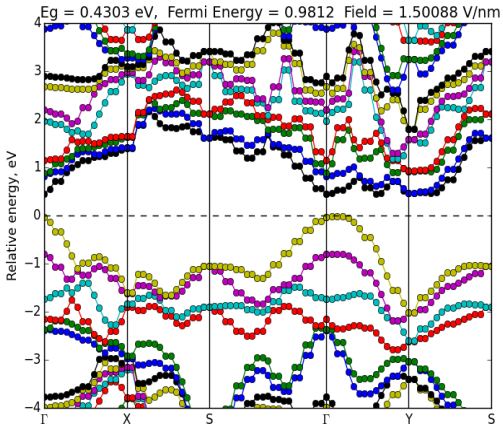

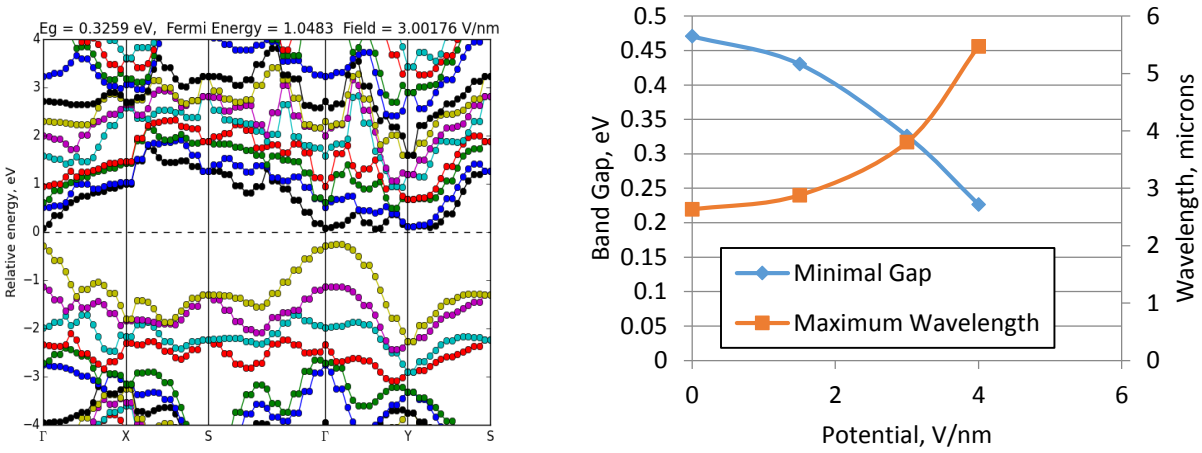

Figure 8 Bandstructures of bilayer black phosphorus with zero electric field (top-left), 1.5 V/nm (top-right) and 3 V/nm (bottom-left).

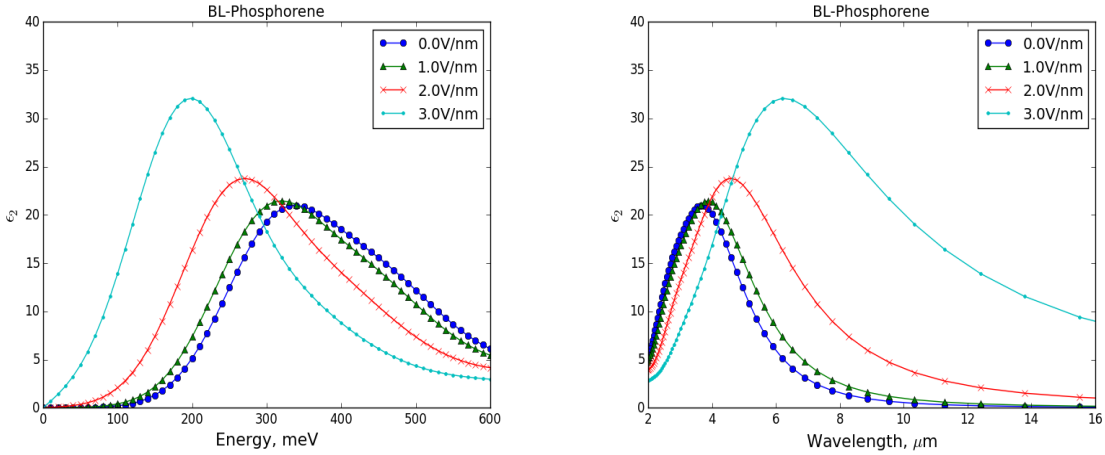

Figure 9 Calculated complex dielectric function for four different electric fields as a function of energy (left) and wavelength (right).

Photodiodes employ doping gradients for depletion and majority carrier blocking, which reduces dark current. An effective doping gradient can be formed by joining dissimilar 2D materials as long as the materials have sufficiently different band offsets. To achieve this affect, moiré cell generating software (see appendix) was developed and employed to perform accurate calculations of the bilayer black phosphorus-MoS_2 heterostructure. This heterostructure is expected to exhibit the tunable aspect as shown as shown above, and majority carrier blocking.

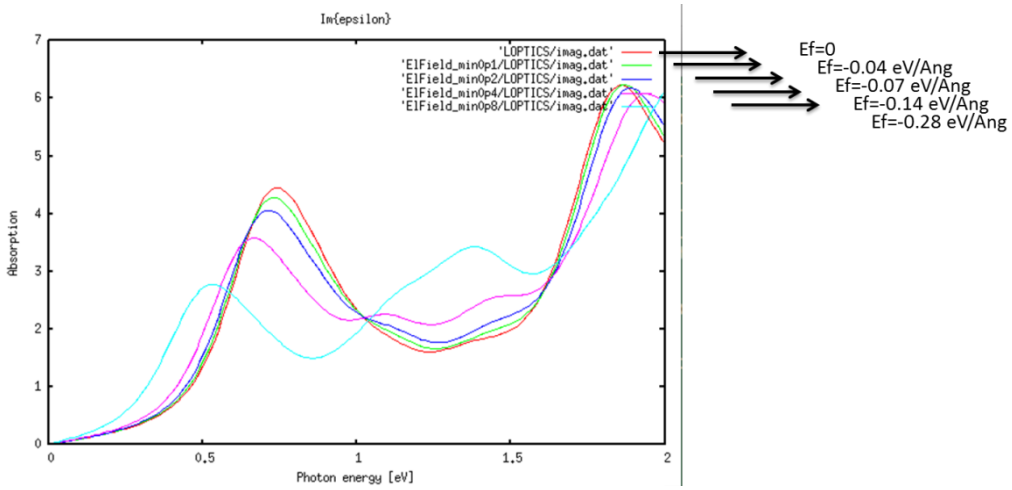

Figure 10 Calculated absorption spectrum for bilayer black phosphorus-MoS_2 heterostructure. The strain on the disssimilar lattices was minimized by using the Moiré cell program (see Appendix A).

As shown in Figure 10, this heterostructure maintains tunable properties at experimentally achievable electric field intensities.

2.3. Tuning the excitonic properties of MoS_2-WS_2 heterostructure with electric field

Transition metal dichalcogenides (TMDC) and their heterostructures bilayers have attracted a lot of attention recently as a promising candidate for photonic and optoelectronic devices. In particular, the MoS_2-WS_2 and $MoSe_2$-WSe_2 heterobilayers have long-lived interlayer excitons as their lowest energy optical excitation line due to their type II band alignment, which is desirable for light harvesting (Hong, 2014; Rivera, 2015). Understanding the response of the interlayer excitonic properties to external electric field and doping is crucial for applications.

2.3.1. Computational approach

The system we studied is the AB-stacked MoS_2-WS_2 bilayer. It can be fabricated by epitaxial growth (Yongji Gong, 2014). The DFT calculation was done with 12 x 12 x 1 k-grid with PBE exchange-correlation functional including the semi-core states of Mo and W. The structure was relaxed, including the van der Waals interaction. The relaxed lattice constant was a=3.18 Å and the layer distance was d=6.21 Å between the Mo and W atoms, which is consistent with previous calculations (Fernández-Rossier, 2013) and close to experimental values (a=3.16 Å, d=6.14 Å for bulk MoS_2 and a=3.15 Å, d=6.16 Å for bulk WS_2).
The many-body calculations include a G_0W_0 calculation of the quasiparticle bandgap, including 18 x 18 x 1 k-grid for the dielectric function and 400 conduction bands. The excitonic effects are included by solving the Bethe-Salpeter Equation (BSE) with a finer k-grid of 90 x 90 x 1. A slab Coulomb truncation was implemented to avoid interactions between periodic images.

2.3.2. Electronic and optical property of intrinsic MoS_2-WS_2 heterostructures.

The DFT bandstructure of MoS_2-WS_2 is shown in Figure 11. The solid and dash line are the bandstructure without and with spin-orbit coupling, respectively. The heterostructure forms Type II band alignment, where the valence band maximum (VBM) at K point is in the WS_2 layer and the conduction band minimum (CBM) is in the MoS_2 layer. The spin-orbit interaction splits the VBM of MoS_2 by 160 meV and WS_2 by 440 meV, and also splits the CBM of MoS_2 by 3 meV and WS_2 by 30 meV.

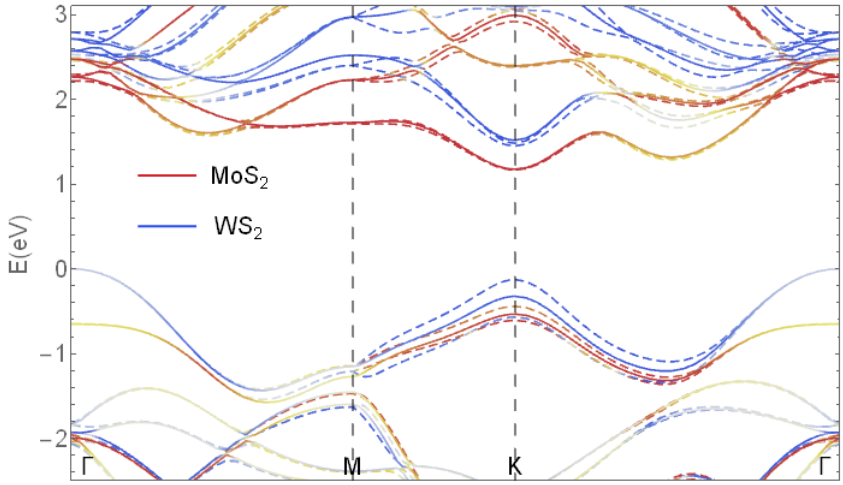

Figure 11 DFT bandstructure of MoS_2-WS_2 heterostructure. The solid and dash lines are band structures without and with spin-orbit coupling, respectively.

The relative band alignment at K point including spin-orbit coupling is shown in Figure 12 in more detail (not to scale). These different bands lead to different optical transitions, including two absorption peaks from intralayer transitions of each layer, and an interlayer transition. Their relative position is shown here. The excitonic states associated with these transitions will be the center of our discussion.

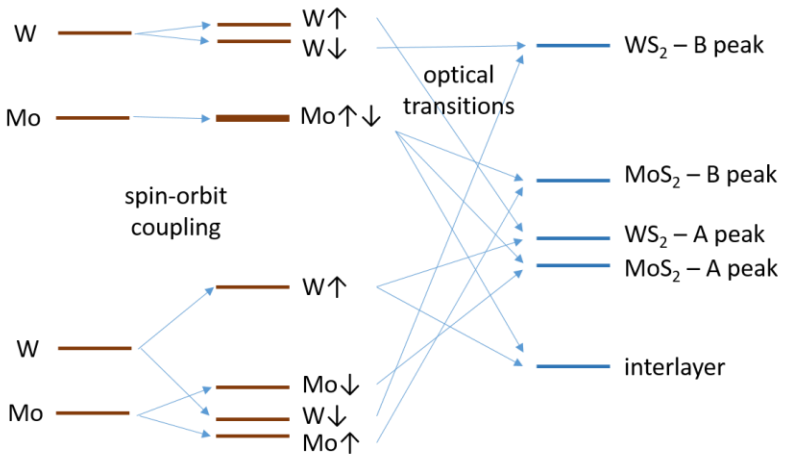

Figure 12 Diagram of the effect of spin-orbit coupling on optical transitions

The DFT calculation is known to underestimate the electronic bandgap. This is corrected by performing the GW calculations, which increases the interlayer and MoS_2 layer bandgap by 0.8

eV, and increases the WS_2 layer bandgap by 0.84 eV. The calculation is done without spin-orbit coupling, but it has been shown that they are usually independent.

Finally, the excitonic effects, which dominate the optical spectrum of 2D TMDCs, are included by solving the BSE and the result are listed in Table 1. For the intrinsic system, we get a binding energy E_b of 0.52 eV for the interlayer exciton, 0.58 eV for the MoS_2 intralayer exciton and 0.56 eV for the WS_2 intralayer exciton. The dipole strength (transition matrix element) of interlayer transition is about 1/8 that of the intralayer transition on the mean-field level, while the e-h interaction increased the strength to about 1/3 that of the intralayer strength. The radiative lifetime of the exciton at zero Kelvins is directly related to the dipole strength by

$$\tau_S^{-1} = \frac{8\pi e^2 E_S \mu_S^2}{\hbar^2 c A_{uc}},$$

where E_S is the energy of the exciton state S, μ_S^2 is the modulus square dipole strength of the exciton divided by the number of k-points, and A_{uc} is the area of the unit cell. The calculated intralayer exciton lifetime of 0.25 ps and 0.19 ps for MoS_2 and WS_2 is in good agreement with a previous calculation (Palummo, 2015) where values of 0.23 ps and 0.19 ps were obtained for monolayers. The interlayer exciton lifetime is shorter than what is reported in that paper because spin-orbit coupling effect, which reduces the interlayer coupling, is not yet included here.

Table 1 Layer specific transition properties for interlayer transitions, MoS_2 transitions and WS_2 transitions.

	Without e-h interaction		exciton			
Transition	gap (eV)	$\|dipole\|^2$	$E_{exciton}$ (eV)	$\|dipole\|^2$	E_b (eV)	Lifetime (ps)
interlayer	2.331	2.23	1.807	0.093	0.524	0.671
MoS_2	2.495	17.09	1.912	0.234	0.583	0.252
WS_2	2.684	19.40	2.123	0.275	0.561	0.193

As we will show, the dipole strength of the interlayer transition, which determines the interlayer exciton lifetime, mainly comes from the coupling between the CBM of the MoS_2 and WS_2 layer, and is therefore tunable by external electric field.

2.3.3. The electric field induced band coupling

A vertical electric field will change the relative band alignment between the MoS_2 and WS_2 layers, thus changing the interlayer coupling between the bands. The electric field-induced charge polarization is shown in Figure 13. The charge polarization partially screens the electric field and leaves the electrostatic potential difference (Figure 14) between the layers much smaller than the bare field times the layer distance. This effect needs to be included when considering the change in the band alignment.

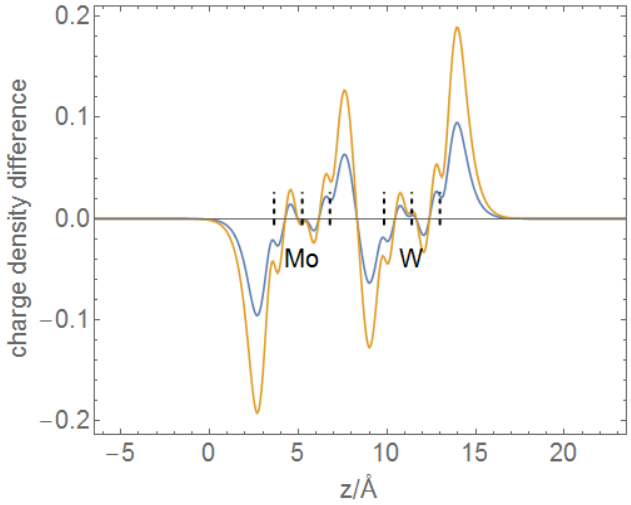

Figure 13 Electric field induced charge polarization of MoS_2-Ws_2 heterostructure as a function of position within the heterostructure. The blue trend represents a 1 V/nm electric field while the yellow line represents a 2 V/nm field.

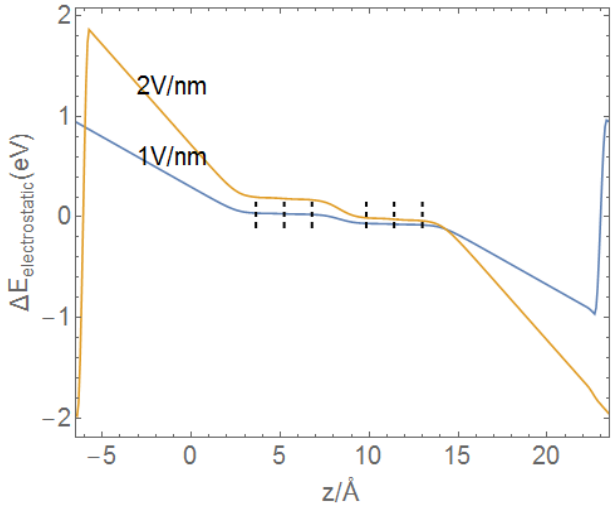

Figure 14 Change in electrostatic potential throughout the heterostructure.

We find that the valence bands originating from the MoS_2 and WS_2 layers around the K point are coupled together. This is shown by the band energy plot as the electric field in

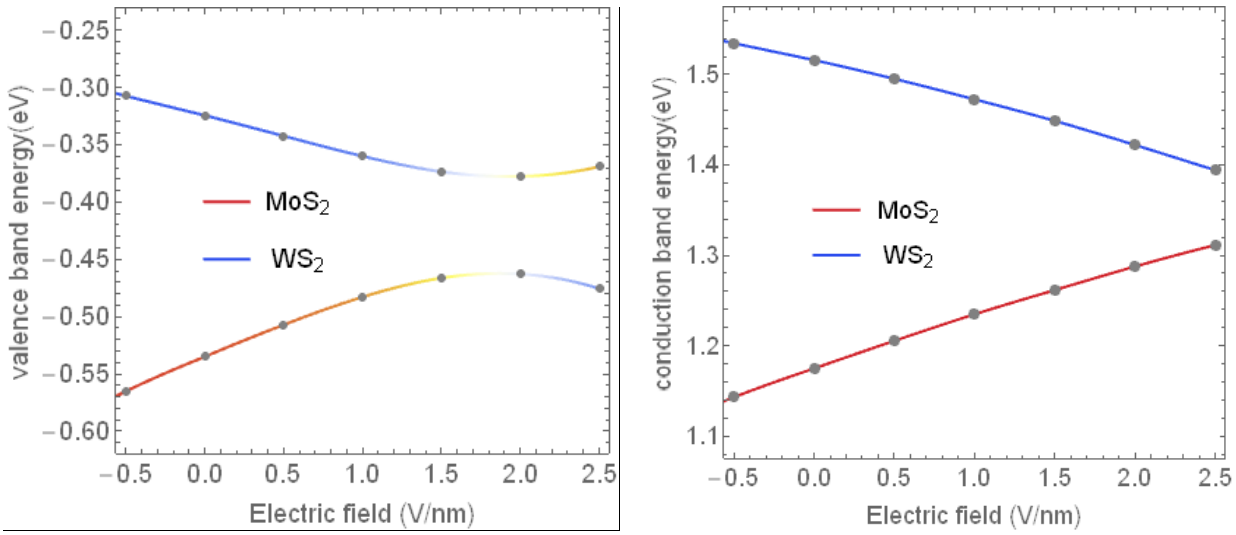

Figure 15. As the electric field reduces the energy difference between the two valence bands, their composition (donated by the color) starts to mix. Near an applied electric field of 1.9 V/nm, the band coupling reaches its maximum. This coupling can be described by a simple 2-by-2 matrix

$$\begin{pmatrix} \epsilon_{Mo} & t \\ t & \epsilon_W \end{pmatrix},$$

where ϵ_{Mo} and ϵ_W are the energy of the valence bands of each layer independently (which changes linearly with applied electric field) and $t = 42\ meV$ is the coupling strength between the layers. On the other hand, the conduction bands from different layers show almost no coupling, and their dependence on electric field is approximately linear.

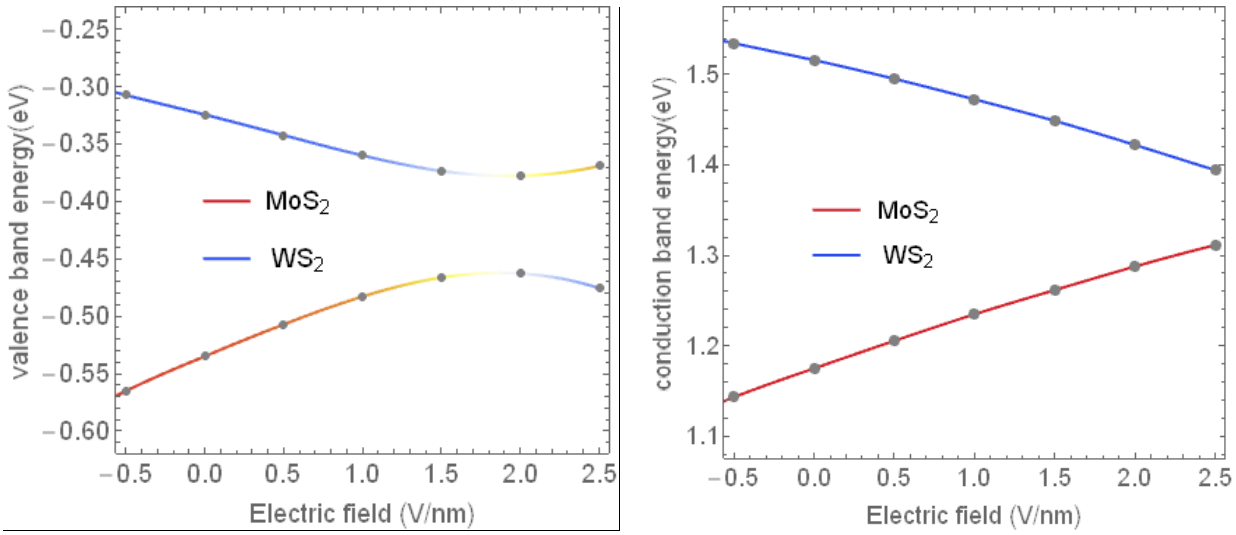

Figure 15 Band-Energy plot for the MoS_2-WS_2 heterostructure as a function of electric field.

The band coupling described by this simple matrix describes most of the dipole strength in the interlayer exciton. Therefore, it shows that the dipole strength and thus the lifetime of the interlayer exciton can be tuned by the electric field.

It should be noted that when spin-orbit coupling is included, only the like-spin bands show this coupling. Without an electric field, the like-spin bands are further apart with spin-orbit coupling, and the interlayer exciton will have a longer lifetime as a result.

2.3.4 The BSE exciton with applied electric field

The dielectric screening of the bilayer system is not very sensitive to electric field strength. Therefore a BSE calculation under different electric fields can be carried out without re-calculating the time-consuming dielectric function. With this simplification, we were able to perform BSE calculation for the system under a range of different electric fields.

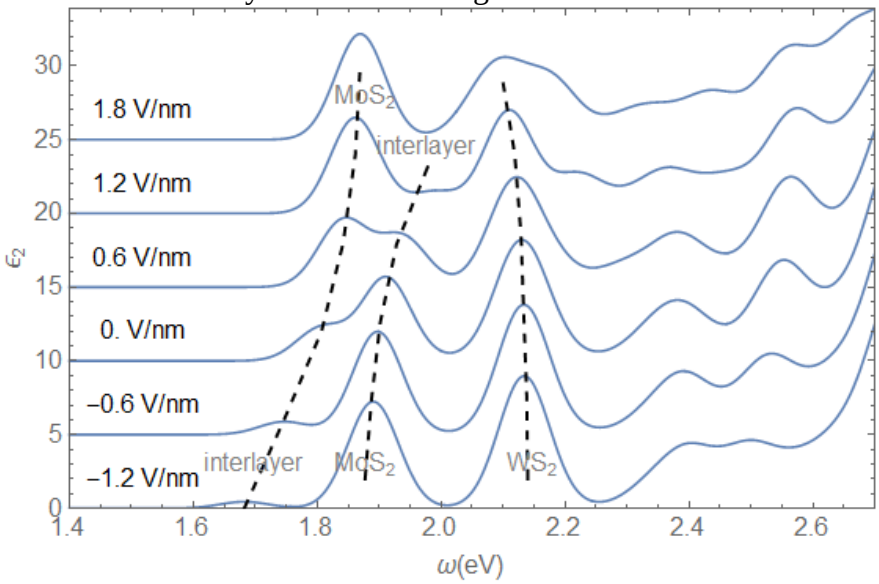

Figure 16 Complex dielectric function as a function of transition energy for several applied electric fields.

The loss function $Im[\epsilon(\omega)]$ in different applied electric fields is shown in Figure 16. These results are preliminary. As the field increases, it is evident that interlayer exciton peak is approaching the MoS_2 intralayer exciton peak, and it is gaining dipole strength due to the increasing coupling between them. As the coupling becomes stronger, the interlayer and intralayer excitons gradually switch position. This verifies the point that vertical electric field can lead to dramatic change in the energy and lifetime of interlayer excitons.

2.4. Dynamical Excitonic Effects in Doped Two-Dimensional Semiconductors

It is well-known that excitonic effects can dominate the optical properties of two-dimensional materials. These effects, however, can be substantially modified by doping free carriers. We investigate these doping effects by solving the first-principles Bethe−Salpeter equation. Dynamical screening effects, included via the sum-rule preserving generalized plasmon-pole

model, are found to be important in the doped system. Using monolayer MoS_2 as an example, we find that upon moderate doping, the exciton binding energy can be tuned by a few hundred meV, while the exciton peak position stays nearly constant due to a cancellation with the quasiparticle bandgap renormalization. At higher doping densities, the exciton peak position increases linearly in energy and gradually merges into a Fermi-edge singularity. Our results are crucial for the quantitative interpretation of optical properties of two-dimensional materials and the further development of ab initio theories of studying charged excitations such as trions. The details of this work are published (Gao, Liang, Spataru, & Yang, 2016).

3. MATERIALS FABRICATION

Recently Sandia National Laboratories has decided to pursue the synthesis of various 2D materials by chemical vapor deposition (CVD). This year's initial efforts saw the assembly and completion of two CVD systems and the initial synthesis of graphene films. Although there is still plenty of work in the future for SNL to truly offer scalable synthesis of 2D films, the ground work has been laid out this year for a path towards large scale synthesis of 2D films as well as synthesis of materials other than graphene, such as MoS_2 and h-BN. In this work we present our current progress of synthesizing graphene and transferring the graphene films onto dielectric substrates.

3.1. CVD growth of Graphene

It was decided that synthesizing graphene on Cu catalyst substrates was the most promising method compared to other metal catalyst such as Au, Ni, Pt or Ir, because of several critical factors (Coraux, et al., 2009) (Li, et al., 2009) (Kondo, et al., 2010) (Gao, et al., 2012) (Li, et al., 2011) (Dato, Radmilovic, Lee, Phillips, & Frenklach, 2008) (Hao, et al., 2013) (Hao, et al., 2016). The growth of CVD graphene has matured greatly over the last 8 years, yielding high quality graphene films, with large grains. The cost of Cu is much less than other precious metals with similar properties (Pt, Au). And graphene films tend to form a self-limiting monolayer film as opposed to metal catalyst such as Ni (Velasco, et al., 2015).

Three catalyst are required for the synthesis of graphene on metal foils by CVD. First is a carbon source, which we have selected methane (CH_4), because it is clean gas source of carbon, compared to gases such as acetylene. Second is a co-catalyst such as hydrogen gas (H_2), which helps reduce the hrydrocarbon molecules. And finally third, a metal catalyst, which we have chosen to be Cu due to the reasons described above. The CVD system is composed of a gas delivery system composed of Ar, CH_4 and H_2 gas cylinders which are connected to mass flow controllers, which can be programed to deliver gas into the system at varying flow rates. The gas is introduced into a quartz reaction chamber, which can reach temperatures up to 1050 C. The chamber pressure is controlled by a fine valve and a baratron, while a vacuum pump is pumping the chamber. The valve can control the pressure from 10 mTorr all the way up to atmospheric pressure.

When the chamber is at high temperature (>1000 C) and CH_4 and H_2 are introduced, then you will begin to form graphene on the surface of the Cu foil. The CH_4 will begin to reduce down to a CH_x and react on a defect site of the Cu foil surface. These initial reactions are nucleation sites and will be and will develop randomly across the Cu foil surface depending on the number of defect sites and the exposure to the gas precursors. Figure 17 shows an SEM image of graphene grains of a few microns forming around the grain boundaries of the Cu foil. The graphene will also form on step edges or any other defect sites on the surface of the Cu foil. For high quality graphene the films need to have high crystallinity, high uniformity and be monolayer. Thus it is important to limit the growth of the graphene to be monolayer, while at the same time reducing the amount of defect sites on the Cu foil, in order to reduce the nucleation density and increase the average graphene grain size of the film. So when growing 2D films these are the parameters that must be controlled and optimized (Li, et al., 2013) (Luo, Kim, Kawamoto, Rappe, & Johnson, 2011) (Li, Colombo, & Ruoff, 2016).

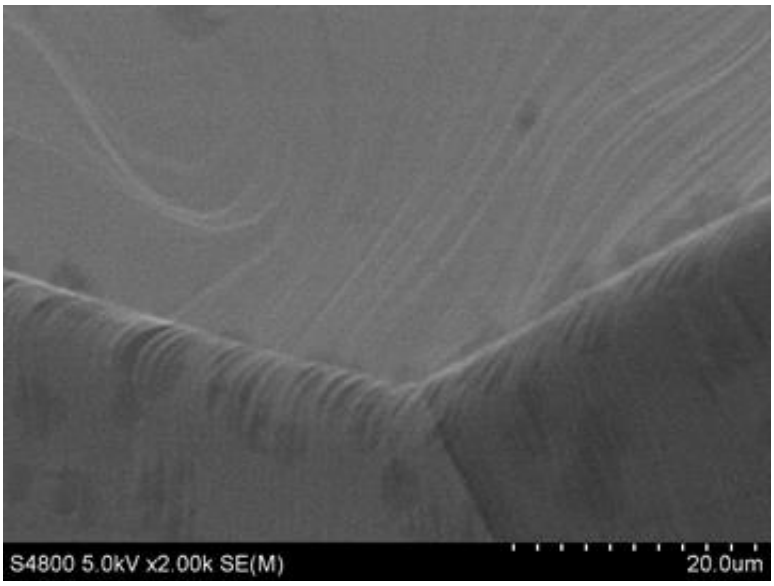

Figure 17 Graphene grains nucleating on the grain boundaries of the Cu foil and on the step edges of the Cu foil.

In order to determine the progress of our films we decided to initially compare it to commercially purchased graphene films from ACS Materials. They offer a graphene film that has already been etched and on a PMMA handle, which is ready for transfer. When comparing the films, we use 3 criteria, 1) the grain size of the films, 2) the uniformity and 3) the Raman spectra. Figure 18 below shows our comparison of our initial optimization recipes and the ACS materials graphene. Figure 18a shows a single layer graphene island with grain size of up ~50 microns, while Figure 18b shows an ACS film, with bilayer regions across the monolayer film. While the bilayer films appear to be less than 10 microns, we can assume the grain size of the monolayer films in the ACS materials is the average distance between closest bilayer regions, as the bilayer regions will share the same nucleation site of the monolayer grains. Thus we can see that the ACS grain size is between 10-15 microns in size, about 3 times smaller than the SNL synthesized graphene. As far as uniformity you can see from the Figure 18a-d that the ACS graphene has many bilayer regions scattered across its monolayer film as well as many wrinkles, while the SNL graphene islands shows no bilayer regions and just a clean monolayer film. In the Raman mapping of the 2D area peak in Figure 18c there are only small regions of bilayer graphene at the edges of the graphene grains, where they appear to have folded over during the transfer. When the graphene is grown to coalesce into a continuous film (longer growth time), then these folded edges will not appear. Finally, the Raman spectra show comparable low D peaks in Figure 18e and Figure 182f , while the ACS material shows spectra for the multilayer regions in the film, while non on the SNL graphene film.

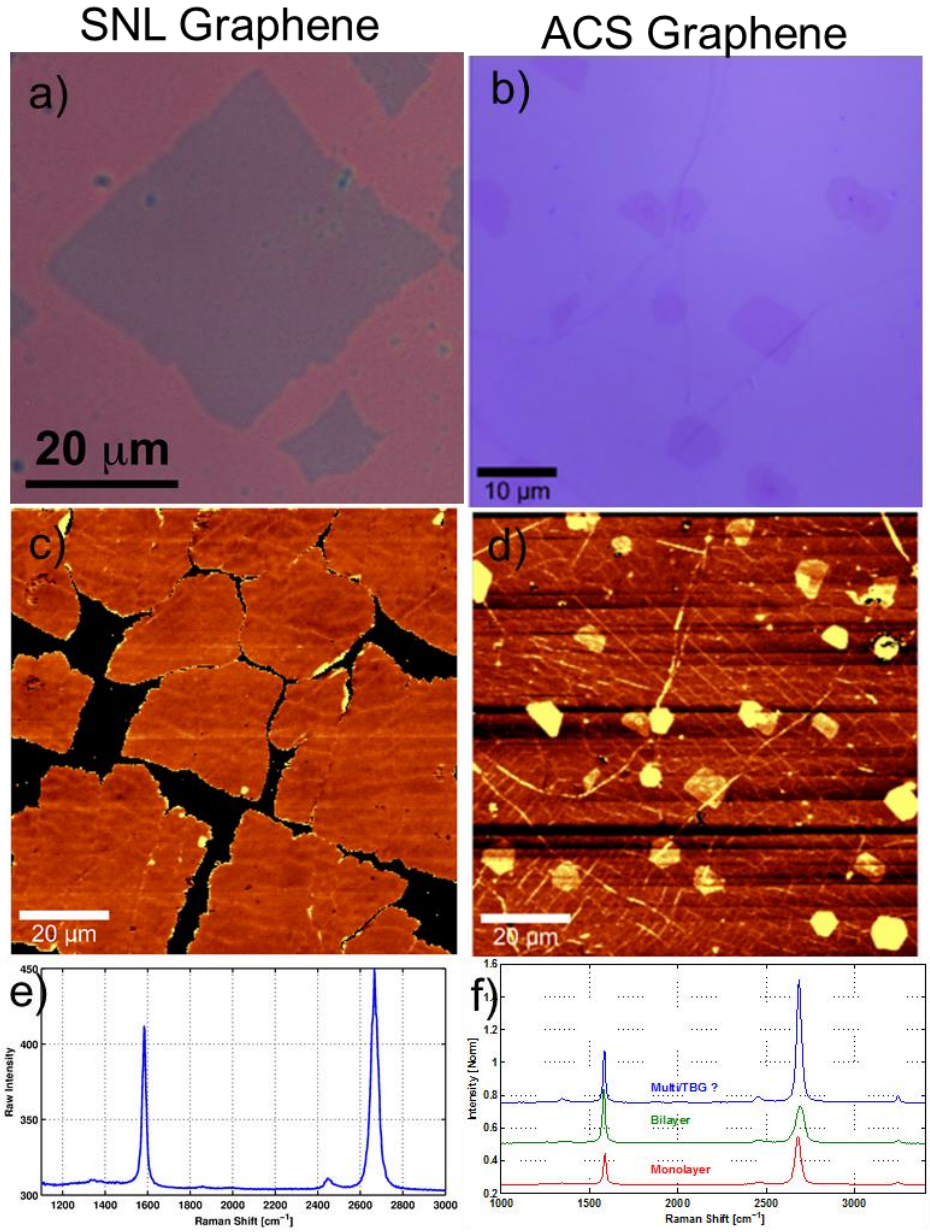

Figure 18 Comparison of SNL graphene vs commercially purchased ACS Materials graphene. SNL graphene a) optical image, c) 2D peak area Raman map and e) single point Raman spectra. ACS materials b) optical image, d) 2D peak Raman area map and f) single point Raman spectra of monolayer, bilayer and multilayer.

3.2. MoS_2 CVD setup and Growth

For the synthesis of MoS_2 film the CVD setup is a little bit more complicated, than is the case for a graphene CVD setup. In the case of MoS_2, the CVD components are the same except that there are now 2 powder precursors, sulfur and MoO_3. Initially the MoO_3 powder needs to be heated up and thin films will be deposited directly onto a dielectric substrate. Next Sulfur and H_2 gas are introduced to reduce and replace the MoO_3 films down to MoS_2 films (Ionescu, et al., 2014).

Since the powder precursors are introduced in the chamber at the beginning of the synthesis but required to be vaporized at different times, a controlled heat source for both precursors are needed. Figure 19, shows a schematic of our MoS_2 tube furnace setup. The MoO_3 powder is put in a crucible in the middle of the tube furnace with the temperature of the tube furnace controlling the vaporization of the MoO_3 onto the substrate, which is placed slightly downstream the tube. The S powder is positions upstream and far enough away that the heating of the tube furnace does not heat up the sulfur crucible. The sulfur crucible is connected to a heating source which is powered by a current source. The sulfur can then be vaporized when the MoO_3 film has been deposited and crystallized on the substrate surface. This allows careful control of both sources without interference from either heat source.

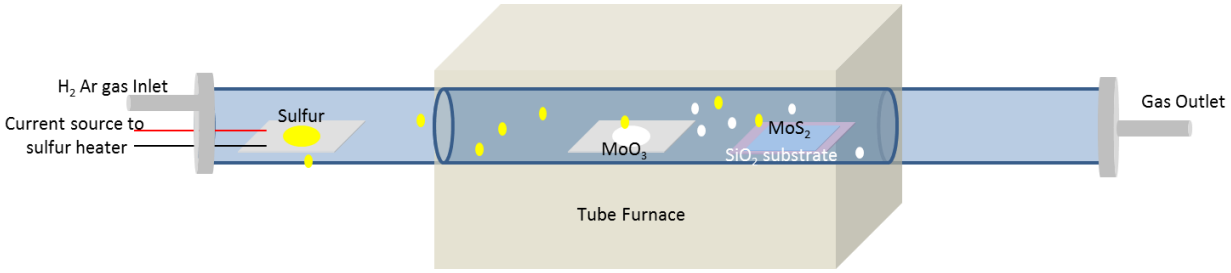

Figure 19 Cartoon of the MoS_2 growth system.

In conclusion, we have demonstrated the setup of 2 CVD furnaces and the growth of graphene films on Cu foils. We have also done the initial optimization on our graphene growth recipes to yield graphene films of higher quality that that is available commercially through ACS Materials. We plan to further improve our graphene films and to also introduce the capability to grow MoS_2 films, which will further expand our 2D material capability.

4. MATERIALS CHARACTERIZATION

4.1. Instrumentation Development and Laboratory Testing

Common techniques for identifying 2D materials include fluorescence spectroscopy, Raman spectroscopy and atomic force microscopy. For exfoliation-based techniques, we started with a widefield microscope. This allowed us to identify potential flakes of interest. It did not allow for identification of number of layers or type of material. This setup was used to place flakes with micron-scale precision. Once locations of interesting flakes were identified, the samples were placed on the laser scanning confocal microscope.

4.1.1. LSCM with imaging, fluorescence and Raman

The LSCM developed for this project is capable of reflectance imaging, fluorescence spectroscopy and Raman spectroscopy, down to approximately 300 cm^{-1} (Figure 20). It employs a 532 nm DPSS laser which is scanned by a two axis galvanometer. The beam goes through a relay and the back aperture of the microscope objective is scanned (0.95 NA, 40X, Nikon microscope objective). The microscope objective is translated with a piezo and the back-reflection was monitored for autofocus and relative distance measurement. The reflected light (and backscattered and photoluminescence) is then de-scanned by the galvanometer mirrors, and is focused on a pinhole or spectrometer. These pinholes enable measurement of material properties with high spatial resolution. High quality dichroic beam splitters and long pass filters are used to achieve low wavenumber Raman measurements.

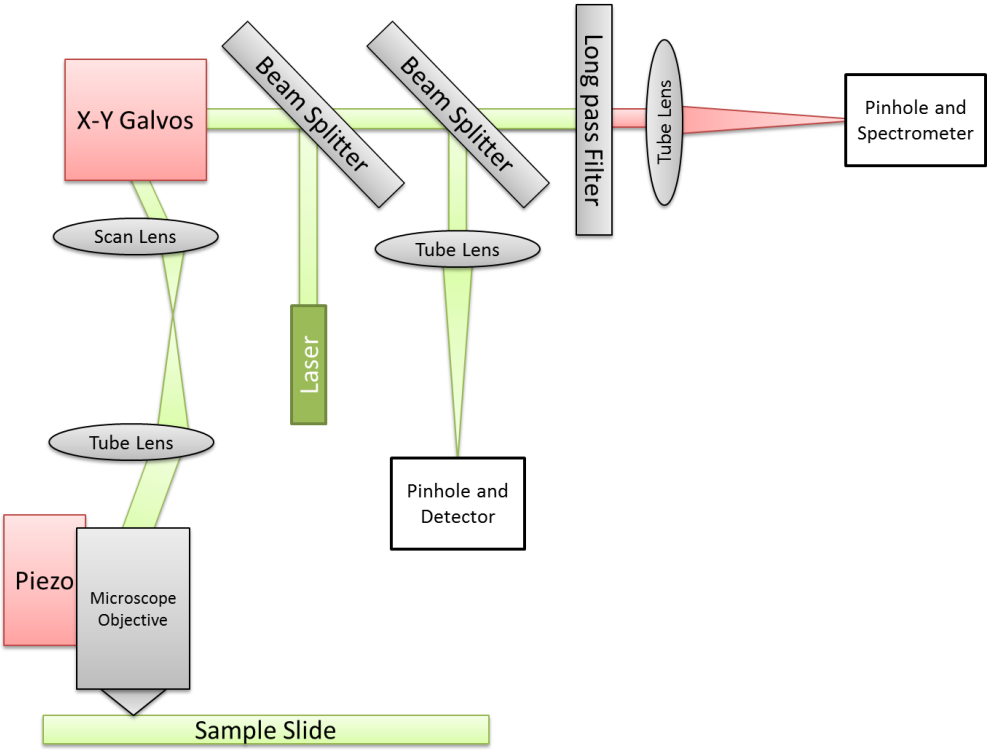

Figure 20 Diagram of LSCM developed to study 2D materials.

The user interface for the LSCM was written in LabView and is shown in
Figure 21. This user interface allows one to capture images and point the laser to a location on the image with the yellow cursor, also shown on the image in
Figure 21. This allows for precise identification of locations for spectroscopic data collection (Figure 22).

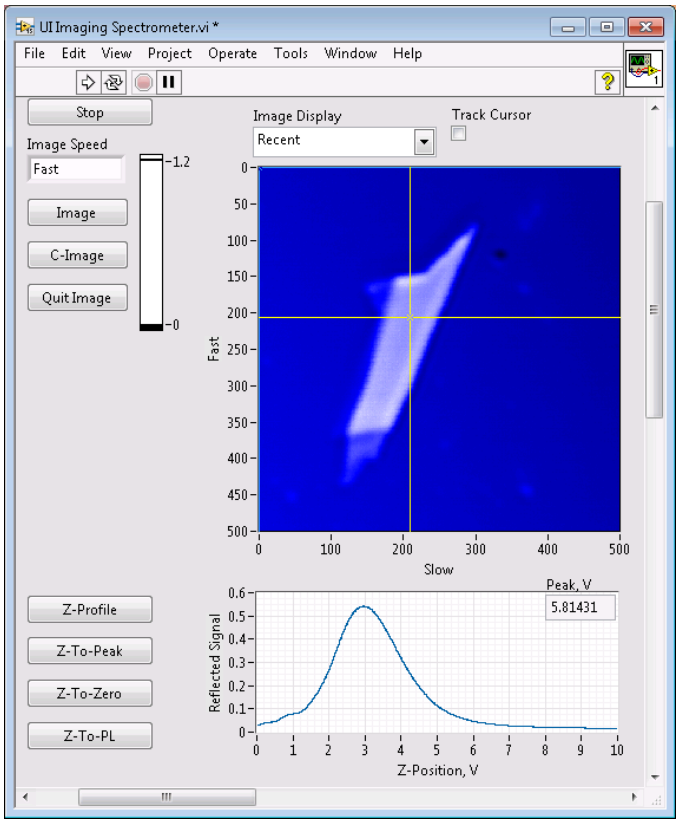

Figure 21 Screenshot of the user interface used to control the LSCM. Imaging options for single and continuous readout, as well as autofocus functions, are located on the top-left and bottom-left, respectively.

Background spectra were found to be essential to obtaining spectra of reasonable quality. Collection of background data involved turning off the laser and accumulating dark current. Subsequently the dark bias data were subtracted from the signal for each pixel in the dataset. Furthermore, application of the same integration time for background and signal results in better spectra. This is likely because of integration time-dependent artifacts in the analog-to-digital conversion in the spectrometer. Simply scaling the background and signal is not adequate.

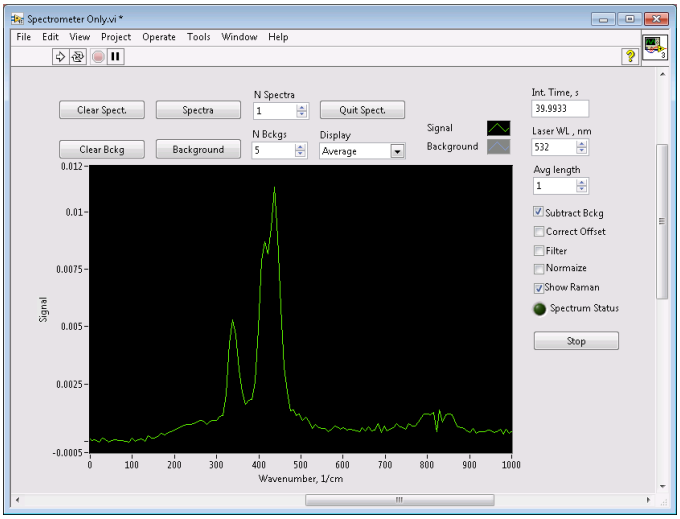

Figure 22 Screenshot of the user interface used to control the spectrometers. This program allows for configuring integration time and the acquisition of multiple backgrounds and spectra for averaging.

The spectral response was measured with a Thorlabs CSS200 compact spectrometer. This spectrometer provides better than 2 nm spectral resolution (FWHM) and integration time of up to 60 seconds.

4.1.2. Spectral Response Instrument

While monochrometer-based spectral response measurements are conceptually simple and can provide effective measurements they suffer limited wavelength range, inefficient light throughput and poor portability. Our experimental approach required a bright source to be fiber coupled for feed-in to the AFM instrumentation. The anticipated response was between one and five microns. A FTIR approach was selected for portability, simplicity and spectral range. This setup is diagramed in Figure 23.

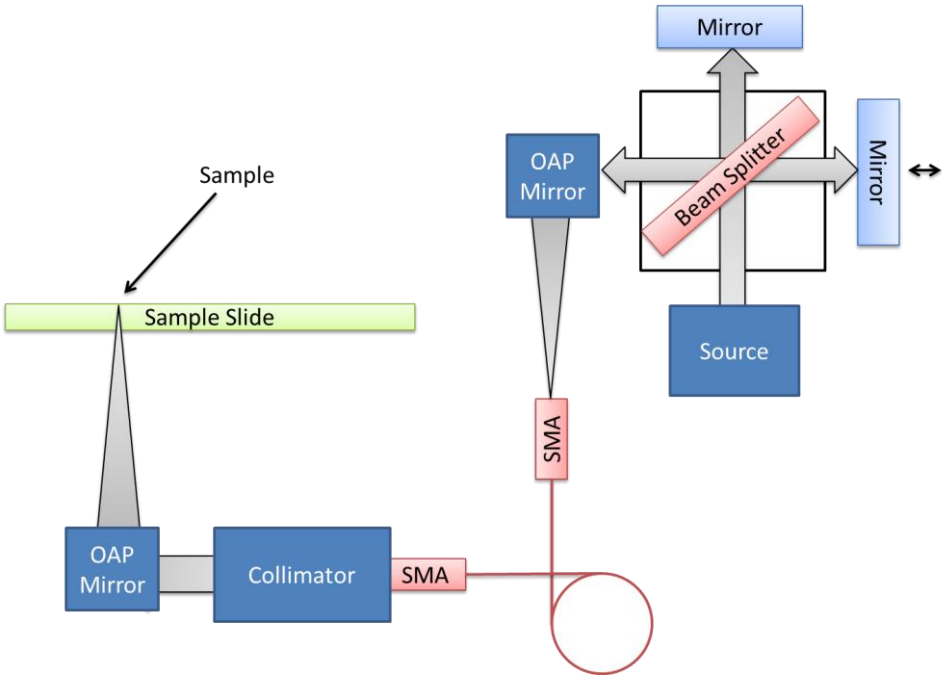

Figure 23 Block diagram of FTIR spectral response instrumentation.

The moving mirror encodes spectral information into the light source. Silver mirrors were selected to cover the SWIR band. A 100 microns travel piezo actuator stage was used to move the mirror. The effective path length of the interferometer was therefore 200 microns and the approximate spectral resolution was approximately 10 nm.

4.2. Graphene Characterization

Large Area Graphene samples were grown by Chemical Vapor Deposition (CVD). The samples were transferred to Silicon Oxide and subsequently characterized with Raman spectroscopy. Raman spectroscopy provides a simple method for identification of graphene, as shown in Figure 24.

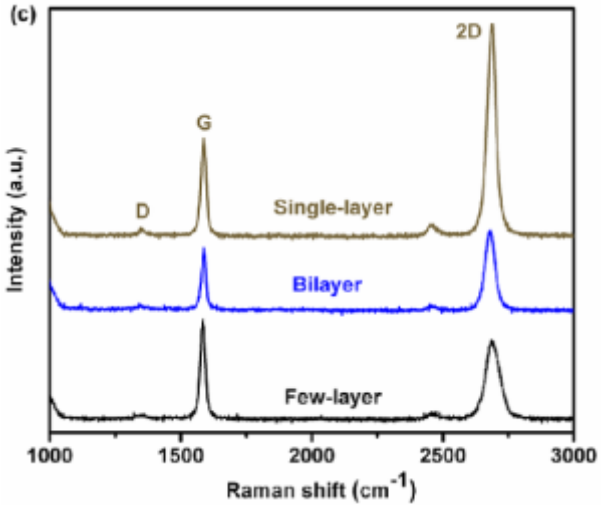

Figure 24 Raman spectra from single-layer graphene, bilayer graphene and few-layer graphene. In single-layer graphene the "2D" peak has roughly twice the intensity of the "G" peak. Figure taken from (benphysics, 2016).

Samples were imaged under a wide field microscope and Raman spectra were acquired at nine different locations (Figure 25). The three samples we studied predominantly showed the single-layer graphene signature. These results provided confidence in the growth technique and its subsequent use.

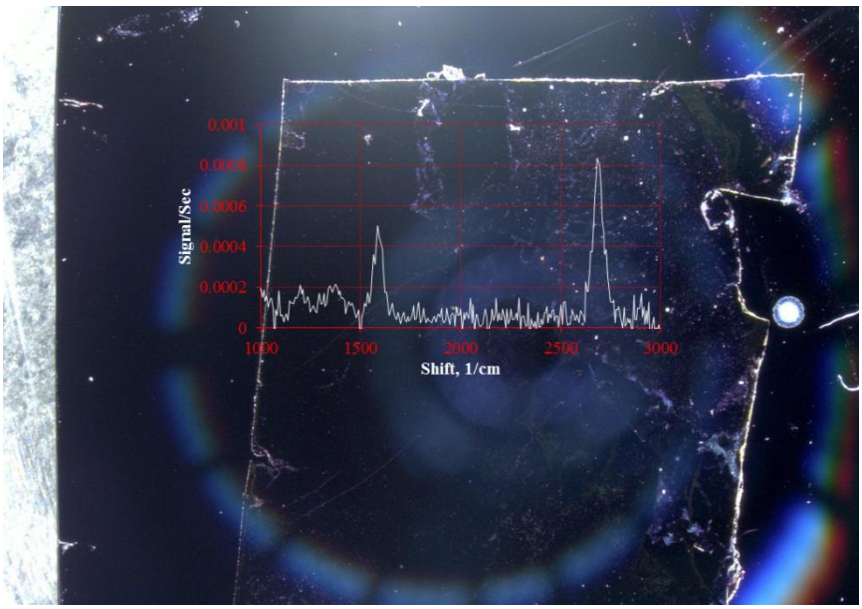

Figure 25 CVD grown graphene image and example Raman Spectrum.

4.3. MoS_2 Characterization

MoS_2 samples were prepared by mechanical exfoliation as described by (Andres, et al., 2014). Samples were placed onto various substrates and Photoluminescence was measured. Stronger photoluminescence is observed from monolayer than multilayer MoS_2 (Eda, Yamaguchi, Voiry, Fujita, Chen, & Chhowalla, 2011).

4.4. Conductive Tip Measurements with Atomic Force Microscopy

To characterize the photo-generated current in a novel 2D material film, at least two electrical contacts are required. Since our samples consist of isolated individual flakes, randomly positioned on surface, depositing surface electrodes would require electron beam lithography. Electron beam lithography is extremely expensive and time consuming, requiring complex coordination between characterization spectroscopies that are used to confirm the material and optical properties of the flake and write locations used by the lithography tool. This coordination is often accomplished with a fiducial reference grid, which requires additional lithography. To circumvent the complexities associated with electron beam lithography, we are using conductive atomic force microscopy (C-AFM) to characterize the photo-response of 2D material flakes, primarily MoS_2 and black phosphorous, deposited on a conductive substrate that is optically transparent.

An atomic force microscope (AFM) is a versatile tool that characterizes both morphology and material properties of a surface by measuring the near-surface forces acting on a nano-scale tip. Since nano-scale is used, the AFM achieves extremely high lateral and morphological resolution (< 10 nm). This extreme resolution makes AFM an ideal tool for characterizing small isolated flakes of novel 2D materials. To perform C-AFM, a conductive tip is brought in to physical contact with the sample surface. By applying a voltage to the tip (or sample), the electronic properties of the sample can be determined by measuring the current flowing through the junction using a preamplifier. Upon raster scanning the tip across the surface, a map representing current flow through each point is generated and can be correlated with surface morphology. For our experiments, the 2D material flakes are deposited on a transparent electrode, such as Indium-Tin-Oxide (ITO) and multilayer graphene (MLG). Using a conductive supporting substrate forms one of the two electrical contacts required to extract current. When the conductive tip is brought into physical contact with the 2D material, forming the second contact, the electronic properties of the junction can be measured.

Figure 26 shows a schematic of the C-AFM setup used to characterize the photo-response of 2D material flakes. The sample rests on a sample holder with an aperture that allows underside illumination. A mirror, located directly under the aperture, allows for the illumination source to be positioned off to the side. The electrical connection to the sample is established using copper fingers on the sample holder. The entire assembly rests on a Z stage that is used to position the sample in close proximity to the scanning tip. Located directly above the sample/holder is the AFM head (tip, piezo-scanner, and optical force feedback system). Figure 26 shows a photograph of the implemented systems.

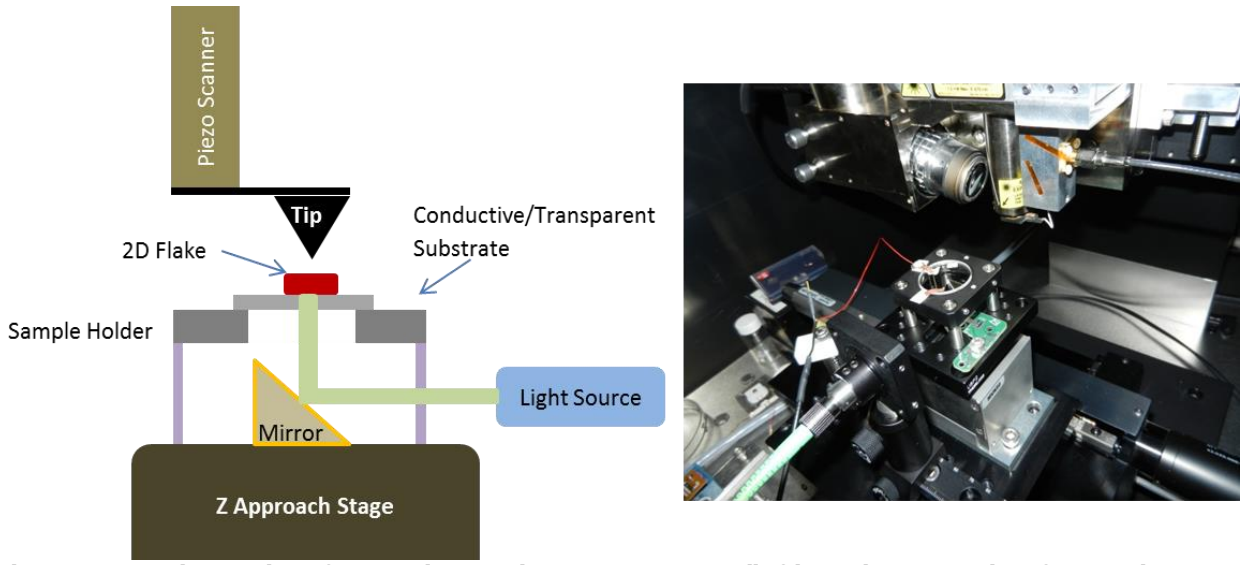

Figure 26 Schematic of experimental C-AFM setup (left). Photograph of actual setup implemented in a commercial AFM system (right).

Figure 27 shows the results of our first attempt to map current as a function of lateral position for a thick flake of MoS_2 deposited on an ITO substrate. The current map in Figure 27 shows the ITO region, off of the MoS_2 flake, is conductive (brighter colors) compared to the MoS_2 region where there was little to no conduction (darker color). This is to be expected due to the thickness of the MoS_2 (> 250 nm). Figure 28 shows the topography (2D and 3D) of a thinner MoS_2 flake, ~ 60 nm thick, deposited on MLG. Work is still ongoing to characterize the electrical response of the thinner flake. This initial work, however, demonstrates that C-AFM can be used to make electrical contacts to thin 2D materials and will be a useful tool for future investigations.

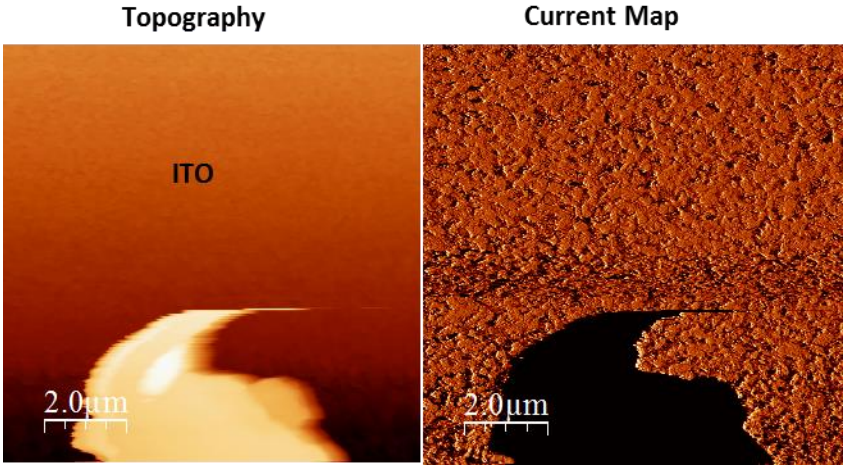

Figure 27 CAFM data for thick MoS_2 flake. Left: Topographic image. Right: Current map.

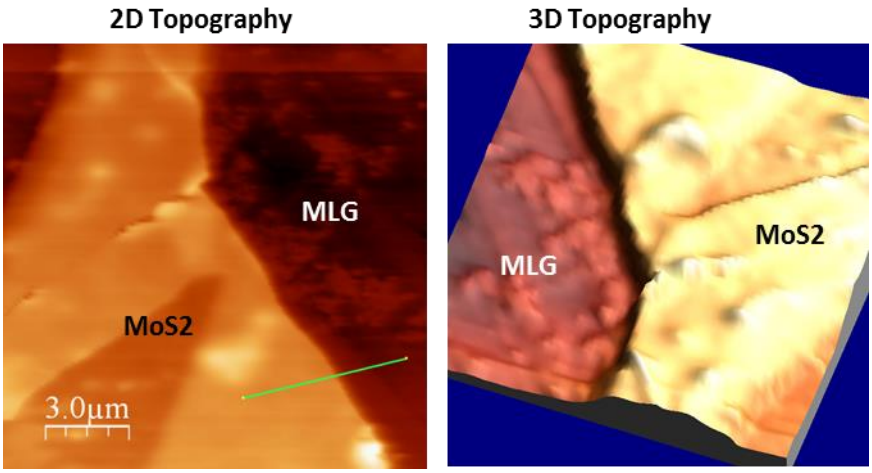

Figure 28 Topography of thin MoS_2 flake.

The unexpected challenge associated with this approach is that it requires placement of 2D material samples onto a transparent conductor. Typical exfoliation techniques target dielectric surfaces such as SiO_2 or HfO_2. Initial experiments involved attempting to exfoliate MoS_2 onto ITO (Indium-Tin-Oxide). The MoS_2 tended to release from the ITO easily. The subsequent experiments attempted to place MoS_2 onto Graphene samples. A similar affect was observed, where the MoS_2 failed to adhere to the graphene surface.
Whether exfoliating onto quartz, SiO_2 or HfO_2, (low and high-k dielectrics) 2D materials tend to exfoliate easily. However, exfoliation onto conductors proved difficult. The difference in tendency to exfoliate onto dielectrics and conductors may have to do with the initial bond mechanism. A potential explanation is that the initial bond requires static force to exfoliate a portion of the sample. We found that MoS_2 flakes exfoliate onto graphene at less than 1% of the rate of exfoliation onto dielectric materials. When exfoliating onto dielectrics there are abundant potential samples to select from, but when exfoliating onto conductors there might only be one or two to choose from. Significant improvement to the efficiency of 2D material transfer onto transparent conductors would be a breakthrough in the experimental approach and field of research.

5. CONCLUSIONS

This exploration of 2D-materials for remote sensing applications involved materials modeling, instrumentation development, fabrication and characterization. Modeling served as an effective way to down-select from a large number of materials. New, high-fidelity modeling approaches were demonstrated and published. Modeling indicated that black phosphorus exhibits electrically tunable absorption properties. If realized and producible in large area formats, this would be a breakthrough for remote sensing technologies.

Instrumentation developed for the fabrication and identification of 2D materials included a widefield microscope, a laser scanning confocal microscope and an instrument for measuring spectral response. The widefield microscope was designed with 3-axis translation stages, enabling one to view the exfoliation of materials in real time and allowing for precision placement of samples. The laser scanning confocal microscope allowed the user to locate flakes on films, image the samples, measure the relative thickness within approximately 50 nm and perform spectroscopic characterization, including photoluminescence and Raman spectroscopy. The spectral response instrument was designed and assembled for characterization of the relative response of materials in the C-AFM approach.

2D materials were fabricated by chemical vapor deposition and mechanical exfoliation from commercially sourced, bulk crystal samples. While exfoliated materials tend to perform better than others, electrically, exfoliation is not a valid approach for large area fabrication. Graphene was grown by chemical vapor deposition and characterized. A MoS_2 chemical vapor deposition furnace was developed as well. Because of the difficulties associated with exfoliating onto conductors, we see growth and transfer of MoS_2 films as a primary next step. A new technique for large area fabrication of black phosphorus was also explored.

The bilayer black phosphorus-MoS_2 heterostructure was selected as a primary device of interest. Modeling of bilayer black phosphorus suggested strong change in the spectral absorption with change of the perpendicular electric field. Addition of MoS_2 is expected to form a P-N junction for majority carrier blocking.

Atomically thin materials that are stable at room temperature offer a relatively new and fruitful area of research. As these materials attract more scientific and commercial interest, large area fabrication of high-quality materials will become possible and device integration will become feasible. Such devices are expected to offer capabilities far exceeding those of bulk materials.

6. REFRENCES

Andres, C.-G., Michele, B., Rianda, M., Vibhor, S., Laurens, J., Herre, S., et al. (2014). Deterministic transfer of two-dimensional materials by all-dry viscoelastic stamping. *2d Materials, 1*(1), 011002.

Bablu Mukherjee, F. T. (2015). Complex electrical permittivity of the monolayer molybdenum disulfide (MoS2) in near UV and visible. *Optical Materials Express, 5*, 447-455.

benphysics. (2016, September 6). *Quantum Frontiers*. Retrieved 9 9, 2016, from https://quantumfrontiers.com/2013/09/06/graphene-gets-serious/

Coraux, J., Engler, M. , Busse, C., Wall, D., Buckanie, N., Meyer ZuHeringdorf, F. J., et al. (2009). Growth of graphene on IR (111). *New Journal of Physics, 11*(2), 023006.

Dato, A., Radmilovic, V., Lee, Z., Phillips, J., & Frenklach, M. (2008). Substrate-free gas-phase synthesis of graphene sheets. *Nano letters, 8*(7), 2012-2016.

Deslippe, J., Samsonidze, G., Strubbe, D. A., Jain, M., Cohen, M. L., & Louie, S. G. (2012). BerkeleyGW: A massively parallel computer package for the calculation of the quasiparticle and optical properties of materials and nanostructures. *Computer Physics Communications, 183*(6), 1269-1289.

Eda, G., Yamaguchi, H., Voiry, D. , Fujita, T., Chen, M., & Chhowalla, M. (2011). Photoluminescence from Chemically Exfoliated MoS2. *Nano Letters, 11*, 5111-5116.

Fernández-Rossier, K. K. (2013). Electronic properties of the MoS2-WS2 heterojunction. *Phys. Rev. B, 87*(075451).

Gao, L., Ren, W., Xu, H., Jin, L., Wang, Z., Ma, T., et al. (2012). Repeated growth and bubbling transfer of graphene with millimetre-size single-crystal grains using platinum. *Nature communications, 3*, 699.

Gao, S., Liang, Y., Spataru, C. D., & Yang, L. (2016). Dynamical Excitonoc Effects in Doped Two-Dimensional Semiconductors. *Nano Letters*.

Hao, Y., Bharathi, M. S., Wang, L., Liu, Y., Chen, H., Nie, S., et al. (2013). The role of surface oxygen in the growth of large single-crystal graphene on copper. *Science, 342*(6159), 720-723.

Hao, Y., Wang, L., Liu, Y., Chen, H., Wang, X., Chen, T., et al. (2016). Oxygen-activated growth and bandgap tunability of large single-crystal bilayer graphene. *Nature nanotechnology*.

Hong, X. a.-F. (2014). Ultrafast charge transfer in atomically thin MoS2/WS2 heterostructures. *Nature nanotechnology, 9*(9), 682-686.

Humberto, T., Lopez-Urias, F., & Terrones, M. (2013). Novel hetero-layered materials with tunable direct band gaps by sandwiching different metal disulfides and diselenides. *Sci. Rep.*

Ionescu, R., Wang, W., Chai, Y., Mutlu, Z., Ruiz, I., Favors, Z., et al. (2014). Synthesis of atomically thin triangles and hexagrams and their electrical transport properties. *IEEE Transactions on Nanotechnology, 13*(4), 749-754.

Kinch, M. A. (2000). Fundamental physics of infrared detector materials. *Journal of Electronic Materials, 29*(6), 809-817.

Kondo, D., Sato, S., Yagi, K., Harada, N., Sato, M., Nihei, M. , et al. (2010). Low-temperature synthesis of graphene and fabrication of top-gated field effect transistors without using transfer processes. *Applied physiscs express, 3*(2), 025102.

Lee, C.-H., Lee, G.-H., van der Zande, A. M., Chen, W., Li, Y., Han, M., et al. (2014). Atomically thin p-n junctions with van dew Waals heterointerfaces. *Nature Publishing Group, 9*(9), 676-681.

Li, Q., Chou, H., Zong, J.-H., Liu, J.-Y., Dolocan, A., Zhang, J., et al. (2013). Growth of adlayer graphene on Cu studied by carbon isotope labeling. *Nano letters, 13*(3), 486-490.

Li, X., Cai, W., An, J., Kim, S., Nah, J., Yang, D., et al. (2009). Large-area Synthesis of high-quality and uniform graphene films on copper foils. *Science*, *324*(5932), 1312-1214.

Li, X., Colombo, L., & Ruoff, R. S. (2016). Synthesis of graphene films on copper foils by chemical vapor deposition. *Advanced Materials*.

Li, Z., Wu, P., Wang, C., Fan, X., Zhang, W., Zhai, X., et al. (2011). Low-temperature growth of graphene by chemical vapor deposition using solid and liquid carbon sources. *ACS nano, 5*(4), 3385-3390.

Lu, N., Guo, H., Li, L., Dai, J., Wang, L., Mei, W.-N., et al. (2014). MoS2/MX2 heterobilayers: bandgap engineering via tensile strain or external electric field. *The Royal Society of Chemistry, 6*(5), 2879-2886.

Luo, Z., Kim, S., Kawamoto, N., Rappe, A. M., & Johnson, A. C. (2011). Growth mechanism of hexagonal-shape graphene flakes with zigzag edges. *Acs Nano, 5*(11), 9154-9160.

Palummo, M. a. (2015). Exciton Radiative Lifetimes in Two-Dimensional Transition Metal Dichalcogenides. *Nano Letters, 15*(5), 2794-2800.

Razavi, B. (2001). *Design of Analog CMOS Integrated Circuits.* McGraw-Hill.

Rivera, P. a. (2015). Observation of long-lived interlayer excitons in monolayer MoSe2-WSe2 heterostructures. *Nature communications, 6*.

Sholl, D. S., & Steckel, J. A. (2009). *Density Functional Theory: A Practical Introcuction.* Hoboken, New Jersey: John Wiley & Sons.

Velasco, M. J., Giamini, S. A., Kelaidis, N., Tsipas, P., Tsoutsou, D., Kordas, G., et al. (2015). Reducing the layer number of AB stacked multilayer graphene grown on nickel by annealing at low temperature. *Nanotechnology, 26*(40), 405603.

Yongji Gong, J. L. (2014). Vertical and in-plane heterostructures from WS2/MoS2 monolayers. *Nature Materials*(13), 1135-1142.

APPENDIX A: MOIRÉ CELL GENERATION

One approach to modeling heterostructures with dissimilar lattice constants accurately is to employ moiré cells. This approach can reduce the amount of strain put on the lattice at the expense of simulating a larger number of atoms (Figure 29).

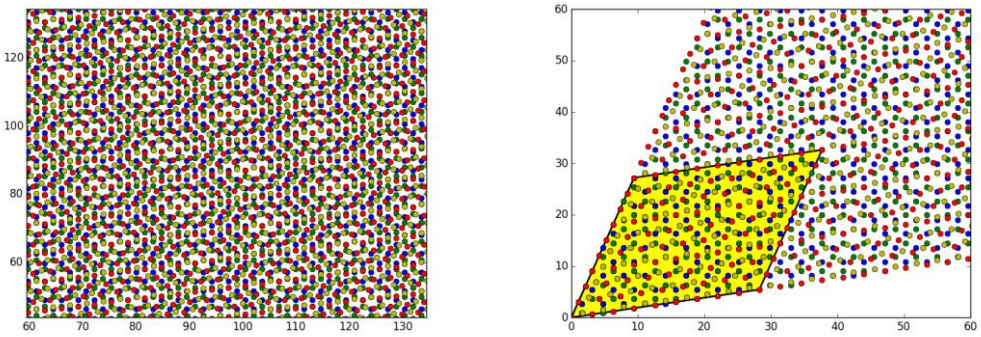

Figure 29 Left: example of moiré patterns generated by two dissimilar hexagonal crystal lattices. Right: Single moiré cell highlighted.

Software for the generation of moiré cells was developed through this project. This software was developed in the python programing using tools in the Chaco application programing interface developed by Enthought. The software allows the user to select four points that make up the corners of a moiré cell (Figure 30). Points are selected by right-clicking on the graph. A yellow point shows up on the plot indicating the last location where the plot was right-clicked. Zoom in and out can be achieved by scrolling the mouse wheel.
Generally one lattice is held fixed and the second lattice is modified to match. The first step is a translation, the second is a rotation and change of scale in the horizontal direction, the third is a change of scale in the vertical direction. If done properly, the fourth lines up and is simply selected to instruct the software what points to apply for file generation.
To generate a moiré cell (Figure 30):

1. Bottom left corner: right-click the location where the two lattices should be shifted to line up. Select and the button “Shift to Point (1)”. The second lattice shifts such that the atoms nearest the indicated point overlap.
2. Bottom right corner: right-click on the location where the two lattices should be rotated and scaled to line up. Select the button “Rotate, Scale to Point (2)”. The second lattice expands or contracts and rotates to match up the two atoms nearest the indicated point.
3. Top right corner: right-click the location where the top right atoms should line up. Select the button “Expand to Point (3)”. The vertical dimension of the second lattice expands or contracts to match the first lattice’s atom closest to the select point.
4. Top left corner: right-click the location of the top left corner of the cell. Select the button “Set Point (4)”.
5. File export: select the button “Create File”. A file is generated to be used as an input to a DFT package.

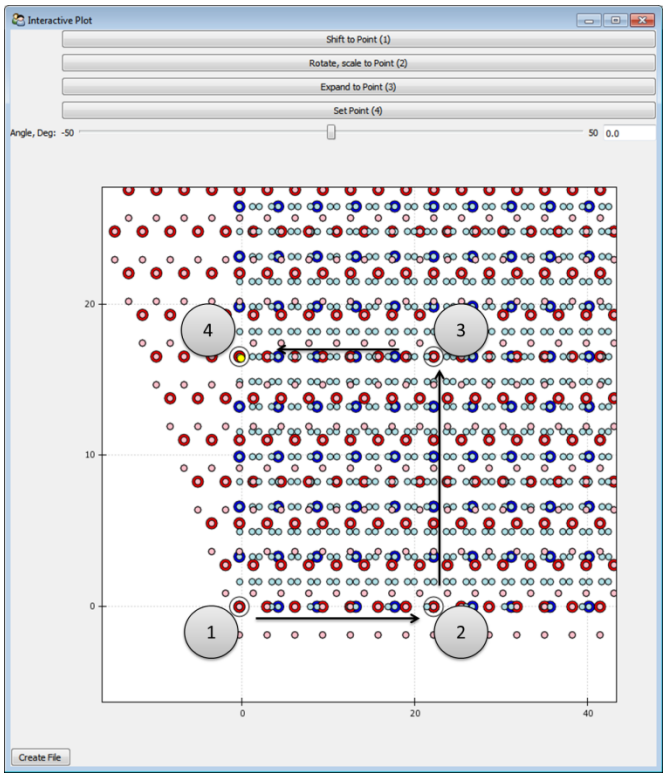

Figure 30 Screenshot of interactive program for the generation of moiré cells based on input atomic positions.

DISTRIBUTION

1	MS0899	Technical Library	9536 (electronic copy)
1	MS0359	D. Chavez, LDRD Office	1911


Sandia National Laboratories